PHYSICAL REVIEW FLUIDS **2**, 113901 (2017)

Leading-edge flow reattachment and the lateral static stability of low-aspect-ratio rectangular wings

Thomas Linehan
Department of Mechanical & Aerospace Engineering, University of Florida, Gainesville, Florida 32611, USA

Kamran Mohseni[*]
Department of Mechanical & Aerospace Engineering and Department of Electrical and Computer Engineering, University of Florida, Gainesville, Florida 32611, USA

(Received 30 January 2017; published 13 November 2017)

The relationship between lateral static stability derivative, C_{l_β}, lift coefficient, C_L, and angle of attack was investigated for rectangular wings of aspect ratio $\text{Æ} = 0.75, 1, 1.5$, and 3 using Stereo-Digital Particle Image Velocimetry (S-DPIV) and direct force and moment measurements. When the product $C_{l_\beta}\text{Æ}$ is plotted with respect to C_L, the lateral stability curves of each wing collapse to a single line for $C_L < 0.7$. For $C_L > 0.7$, the linearity and scaling of C_{l_β} with respect to C_L is lost. S-DPIV is used to elucidate the flow physics in this nonlinear regime. At $\alpha = 10^\circ$, the leading-edge separation region emerges on the leeward portion of the sideslipped wing by means of vortex shedding. For the $\text{Æ} \leqslant 1.5$ wings at $\alpha > 15^\circ$, the tip vortex downwash is sufficient to restrict the shedding of leading-edge vorticity thereby sustaining the lift of the leading-edge separation region at high angles of attack. Concurrently, the windward tip vortex grows in size and strength with increasing angle of attack, displacing the leading-edge separation region further toward the leeward wing. This reorganization of lift-generating vorticity results in the initial nonlinearities between C_{l_β} and C_L at angles of attack for which C_L is still increasing. At angles of attack near that of maximum lift for the $\text{Æ} \leqslant 1$ wings, the windward tip vortex lifts off the wing, decreasing the lateral static stability of the wing prior to lift stall. For the $\text{Æ} = 3$ wing at $\alpha > 10^\circ$, nonlinear trends in C_{l_β} versus C_L occur due to the spanwise evolution of stalled flow.

DOI: 10.1103/PhysRevFluids.2.113901

I. INTRODUCTION

There is increasing interest in developing reliable small-scale unmanned aerial vehicles (UAVs) that provide penetrating surveillance in highly congested and dynamic environments. UAVs of this sort are commonly designed around a low-aspect-ratio (LAR) wing and tend to fly at low speeds requiring high angles of attack to trim. Accordingly, the flow regime is often highly unsteady and dominated by flow separation and transition. In order to maintain high levels of maneuverability in a flexible flight envelope, the aerodynamic and stability couplings associated with LAR flight must be identified outside the canonical attached-flow flight regime.

The three-dimensional vortex topology of LAR rectangular wings at angles of attack involving leading-edge separation has been studied both experimentally and computationally by various groups. The wind tunnel smoke visualizations of Freymuth *et al.* [1] provided some of the first glimpses into the complex three-dimensional vortex structures over steadily translating and maneuvering finite wings. The main structures on the wing consist of a pair of counter-rotating side-edge tip vortices and a leading-edge separation region. At low chord-based Reynolds numbers $\text{Re}_c = O(100)$, the computations of Taira and Colonius [2,3] displayed the leading-edge separation

---

[*] mohseni@ufl.edu

©2017 American Physical Society

region in the form of a recirculatory leading-edge vortex (LEV). The interaction of the tip vortices on the LEV was noted to both enhance lift (by moving the low-pressure core closer to the wing surface) and to stabilize the flow by restricting vortex shedding. Using particle image velocimetry, Yilmaz and Rockwell at $\mathrm{Re}_c = 10\,000$ exposed the importance of axial flow on the initial development of the leading-edge separation region [4] and the occurrence of streamwise-orientated vorticity in the separated region [5]. At Reynolds numbers in the range $\mathrm{Re}_c = O(10^3\text{–}10^4)$, the simulations of Visbal on an $\mathcal{R} = 2$ wing undergoing pitching [6] and heaving [7] maneuvers unveiled the transitional nature of the flow. For both the plunging and heaving maneuvers, the leading-edge separation region develops into an arch-type vortex. Moreover, the tip vortices are noted to undergo vortex breakdown at high angles of attack in the pitching profile and at various stages in the heaving motion. At Reynolds numbers in the range $\mathrm{Re}_c = O(10^4\text{–}10^5)$ various researchers have identified the leading-edge separation region being formed by a Kelvin-Helmholtz instability in the leading-edge shear layer that results in the break-up and shedding of discrete vortices that succumb to turbulence in their downstream evolution [8,9].

The reattachment of edge flow (e.g., the tip vortices and the leading-edge separation region for the rectangular wing) results in nonlinear forces and moments on the wing [8,10–14]. These additional forces attenuate the Reynolds number effects that decrease airfoil [15,16] and wing performance [17–19] during flight at low speeds and low angles of attack. Regarding the aerodynamics at high angles of attack, it is well recognized that LAR wings experience sustained lift and delayed stall [8,9,13,20]. Through the concept of an “effective bound circulation” of the wing, which combines the circulation associated with bound vorticity and the vorticity comprising the leading-edge separation region, DeVoria and Mohseni [21] interpret the sustained time-averaged lift at high incidence to be a result of the induced flows of the tip vortex reducing the generation of opposite-signed “image” vorticity from the trailing edge of the wing.

The stability of the wing is also influenced by the nonlinear forces associated with the tip vortices and the leading-edge separation region. To date, much of the work connecting the complex aerodynamics of LAR wings to stability has focused on longitudinal stability in symmetric flight. Here, it is well recognized that the emergence and growth of the separation region and the strengthening of the tip vortices with angle of attack moves the aerodynamic center continually aft of the quarter-chord point causing increased pitch stability for LAR wings at high lift coefficients [8,13,19].

The stability and performance in cross-flow has drawn more attention in recent years in an attempt to improve handling qualities associated with low-speed flight at low altitudes. In this flight regime, perturbations in sideslip are inevitable as average wind speeds in the atmospheric boundary layer often occur on the order of the vehicle’s forward airspeed [22]. The effect of asymmetric flight on the longitudinal aerodynamics and stability of LAR wings was studied by Shields and Mohseni [23]. It was shown that while the angle of sideslip had little effect on the aerodynamic performance of LAR rectangular wings, increased sideslip results in decreased longitudinal stability for a given angle of attack. More commonly, the angle of sideslip is recognized for its effect on the lateral forces and moments of the wing. Sideslip introduces asymmetries in the spanwise loading that result in stabilizing roll moments that increase with angle of attack. Here the stabilizing roll moment is not simply the result of the arrangement of bound vorticity on the sideslipped wing [24], but also a result of asymmetries in free vorticity on the wing [25]. Ultimately, the large stabilizing roll moments developed in sideslip on wings of decreasing aspect ratio coupled with the “slender” inertia and damping properties of the LAR wing result in unstable stability modes such as wing rock [26,27] and the roll resonance mode [28] that are unique to LAR wings.

Of specific interest to this paper is to elucidate the fluid dynamics associated with a phenomena termed “roll stall” [29], which impacts the lateral static stability of the rectangular wing at high angles of attack. Roll stall occurs when the time-averaged roll moment, hereafter referred to as the nondimensional coefficient C_l, no longer increases with angle of attack but “stalls” at an angle of attack independent of small nonzero sideslip angles, $|\beta| < 20^\circ$. Moreover, the angle of attack of roll stall is not coincident with lift stall. Such trends on rectangular wings differ from what is

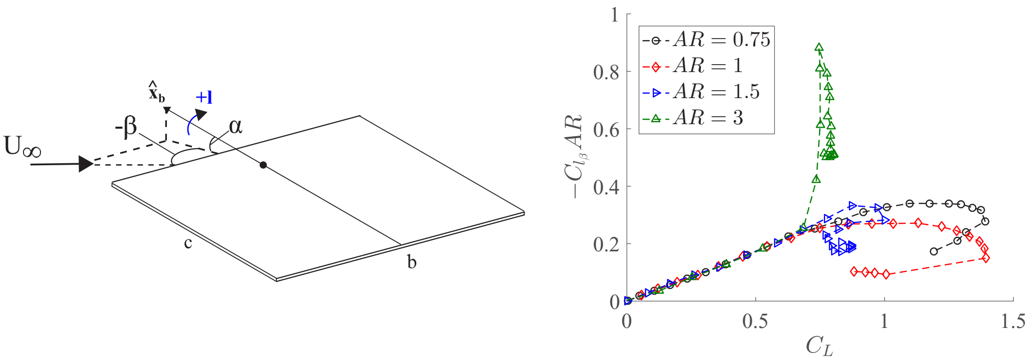

FIG. 1. (Left) Roll moment and wind angle definitions for a rectangular wing of aspect ratio $Æ \equiv b^2/S = b/c$, where b and c are the span and chord, respectively. Roll moment, l, is defined positive clockwise about the vector $\hat{x}_b$, where $\hat{x}_b$ is fixed to the body and directed out the leading edge, parallel to the wing chord. (Right) The negative of the product of lateral static stability derivative and wing aspect ratio, $-C_{l_\beta} AR$, versus the lift coefficient, C_L, for rectangular flat-plate wings of various aspect ratio.

commonly known to occur on delta wings where the reduction of roll moment at high angle of attack is complemented with an abrupt loss in lift due to asymmetric vortex breakdown [30,31].

To analyze the impact of roll stall on lateral stability for the rectangular wing, the static lateral stability derivative, C_{l_β}, is computed in the body axis of the wing at a range of angles of attack from the roll moment data presented in Ref. [29]. Figure 1 plots $-C_{l_\beta} Æ$, versus lift coefficient, C_L, for the rectangular wings of various aspect ratio; recall that a wing is defined statically stable in roll when $C_{l_\beta} < 0$. Incorporating the additional scaling of wing aspect ratio, Æ, collapses the stability curves of the wings of varying aspect ratio to a single line at low-to-moderate lift coefficients, $C_L < 0.7$. In this range, the lateral static stability of the wing increases linearly with increased lift as the wing loading remains asymmetric in sideslip such that increases in lift results in subsequent increases in the stabilizing roll moment. Such collapse is lost at high lift coefficients, $C_L > 0.7$, where the lateral static stability of each wing behaves nonlinearly with respect to lift coefficient. For the $Æ \leqslant 1.5$ wings, lateral static stability stalls at lift coefficients less than $C_{L_{\max}}$. In contrast, the lateral stability of the $Æ = 3$ wing sharply increases at initial angles of attack greater than for which lift has stalled, but sharply declines at higher angles of attack.

As roll stall occurs seemingly independent of lift stall, it is clear that neglecting the impacts of roll stall whether in vehicle or control design threatens to reduce the operable flight envelope of low Æ fliers. This motivates the present investigation into the fluid dynamics of rectangular wings at high angle of attack in sideslip. Of specific interest is to gain insight into the development of flow-field asymmetries that result in roll stall. Stereoscopic digital particle image velocimetry measurements are taken on various Æ wings at zero and nonzero sideslip through a range of angles of attack. Due to the combined importance of the leading-edge separation region and the induced flows of the tip vortices, we analyze the flow field around LAR wings via both streamwise and cross-flow measurement planes.

The paper is organized as follows. The experiment design, equipment, methods, and error estimates are reported in Sec. II. Experimental measurements at $\beta = 0^\circ$ are first reported in Sec. III A followed by measurements in $\beta = -10^\circ$, which are reported Sec. III B. We proceed to interpret the nonlinearities associated with roll stall in Sec. IV and provide concluding remarks in Sec. V.

II. EXPERIMENTAL METHODS

Stereoscopic Digital Particle Image Velocimetry (S-DPIV) is used to retrieve three-component velocity measurements (2D-3C) in both cross-flow and streamwise planes on flat-plate rectangular wings at various angles of attack in sideslip. The experimental setup, as shown in Fig. 2, consists

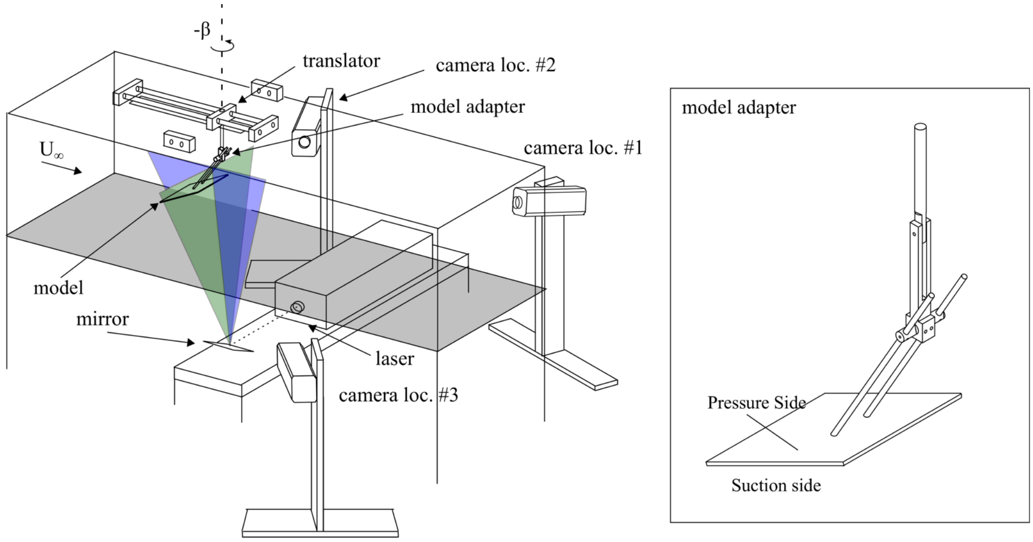

FIG. 2. S-DPIV setup in the wind tunnel test section (left) and a close-up of the model adapter holding the $\mathcal{AR} = 1$ wing (right). The laser sheet for both streamwise and cross-stream measurements are marked blue and green, respectively. The model adapter suspends each model upside down in the test section from two rods that are fastened to the pressure surface of the inclined wing.

of a mounting rig that allows the user to manually set angle of attack, sideslip angle, and linear position. The model is positioned using a motorized translator that is mounted to the top plate of the wind tunnel test section in one of two configurations which allow for model translation in either streamwise or cross-stream directions. For cross-stream velocity field measurements (laser sheet marked green) the motorized translator is mounted as shown in Fig. 2. In this case, streamwise position is adjusted in order to fix the distance between the leeward trailing edge and the laser sheet while angle of attack and sideslip are changed. The motorized translator is mounted orthogonal to the configuration shown in Fig. 2 for streamwise velocity field measurements (laser sheet marked blue). This configuration of the translator allows for streamwise velocity fields to be obtained at various cross-stream locations on the wing.

The models are mounted upside down with two stainless steel rods (6.35 mm diameter) connected on the pressure sides of the wing as to reduce the obstruction of flow reattachment on the sensitive suction side of the wing. Two countersunk set screws connect the models to the mounting rods. The rods are mounted symmetric about the midspan of the wing and spaced approximately 4 cm apart. The angle of attack is adjusted to within $\pm 0.2^\circ$ precision using the set-screwed rotatory pivots on the model adapter. The sideslip angle of the model is adjusted by rotating the model adapter with respect to the translator and set-screwing its angular position. A ruler was used to set the angle of sideslip by measuring the distances between the model's edge and the tunnel side wall. The error in the measurement of sideslip is $\pm 1.2^\circ$, $\pm 1.43^\circ$, and $\pm 2.87^\circ$ for the $\mathcal{AR} = 0.75/1$, 1.5, and 3 wings, respectively.

The high-speed cameras were placed at different locations for cross-stream and streamwise S-DPIV measurements as to maximize the overlapping field of view and combined camera opening angle while minimizing perspective error for both the zero and nonzero sideslip cases in lieu of test section viewing restrictions. The cameras were positioned in locations one and three as shown in Fig. 2 (camera loc. no. 1 and no. 3) with a combined camera opening angle of approximately 60° for cross-stream velocity field measurements. In this configuration each camera had a Scheimflug attachment and was adjusted to meet the Scheimpflug imaging criterion thus aligning the image, object, and lens planes for each camera. In order to resolve the streamwise-orientated flow over the

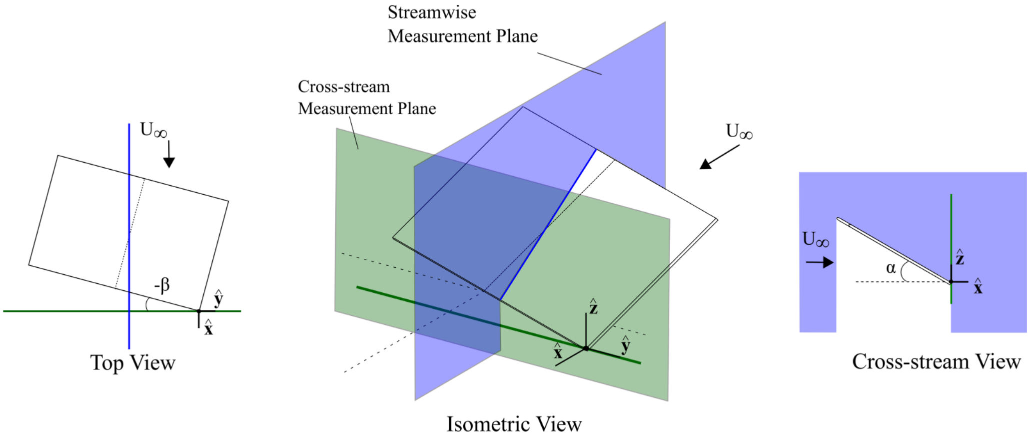

FIG. 3. Measurement planes and coordinate system for S-DPIV flow measurements. Coordinate vectors are defined with respect to the freestream: $\hat{x}$ is defined positive downstream, $\hat{z}$ positive toward zenith, and $\hat{y}$ orthogonal to the freestream by $\hat{z} \times \hat{x}$. The coordinate system origin is fixed to the leeward corner of the sideslipped wing unless otherwise specified. Note that for $\beta = 0^\circ$, the cross-stream measurement plane is coincident with the full trailing edge of the wing, and the streamwise measurement plane is oriented parallel to the chord.

wing, the cameras were positioned in locations one and two as shown in Fig. 2 (camera loc. no. 1 and no. 2) where camera no. 1 had a Scheimflug attachment. The combined camera opening angle in this configuration was approximately 40°.

Figure 3 depicts the location of the measurement planes and the coordinate system definition used throughout the paper. The coordinate system origin is set at the leeward corner of the wing in sideslip unless otherwise specified. Coordinate vector $\hat{x}$ is defined positive in the direction of the freestream and $\hat{z}$ is defined positive towards zenith. $\hat{y}$ is defined positive by the vector cross product $\hat{z} \times \hat{x}$. The cross-stream measurement plane is fixed normal to the wind and is coincident to the leeward wing's trailing corner. At zero sideslip, $\beta = 0^\circ$, the cross-stream measurement plane is parallel to the span of the wing, and the coordinate unit vector $\hat{y}$ is coincident with the trailing edge and points out the right wing.

Streamwise measurements are taken at five evenly spaced $\hat{y}$ locations. At $\beta = 0^\circ$, the streamwise measurement plane is parallel to the wing chord and located at $y/b = [-0.30, -0.15, 0, 0.15, 0.30]$ measured from the origin at the midspan. Here, b is the span of the wing. At $\beta = -10^\circ$, the streamwise measurement planes are located at $y/b = [-0.10, -0.25, -0.40, -0.55, -0.70]$ measured from the origin at the leeward corner.

Rectangular wings of aspect ratio $\mathcal{A}\!\!R = 0.75$, 1, 1.5, and 3 are tested in this experiment. Each model had a 5:1 elliptical leading-edge and square trailing and side edges. Table I lists additional model and flow parameters for each model. The selected model, edge geometries, and free-stream velocities for all tests was chosen to stay consistent with the direct force measurements of Shields

TABLE I. Model and flow parameters.

$\mathcal{A}\!\!R$	c [cm]	b [cm]	t/c	U_∞ [m/s]	Re_c
0.75	15.24	11.43	2.8%	7.72	76 600
1	15.24	15.24	2.8%	7.72	76 600
1.5	12.7	19.05	3.3%	8.66	71 500
3	6.35	19.05	6.6%	18.70	77 200

and Mohseni [29] thereby allowing direct reference of the measured flow fields to mean loads. The chord based Reynolds number, Re_c, was computed based on streamwise S-DPIV measurements of the undisturbed freestream for each tunnel velocity. Cross-stream and streamwise velocity fields are obtained for $\mathcal{R} = 0.75/1$ and $\mathcal{R} = 1.5/3$ wings at angles of attack ranging from $\alpha = 10°–40°$ and $\alpha = 10°–30°$, respectively; cross-stream velocity fields were obtained in 10° increments where streamwise velocity fields were obtained in 5° increments.

A. Equipment

The experiments were conducted in the Engineering Laboratory Design recirculating wind tunnel located at the University of Florida. The test section has a $61 \times 61\ \mathrm{cm}^2$ cross section and is 2.44 m in length. The wind tunnel can achieve freestream velocities ranging from 3–91.4 m/s with a freestream turbulence intensity of 0.12%.

The wind tunnel is seeded with olive oil particles ($\sim 1\ \mu\mathrm{m}$) generated by an atomizer. Olive oil particles are illuminated by a 4 mm thick laser sheet generated by a 20 mJ Nd:YLF laser (Quantronix Darwin Duo, $\lambda = 527$ nm) capable of repetitions up to 10 kHz. The imaging system consists of high-speed CMOS 1 Mpx cameras (Phantom v210/v211, $1280 \times 800\ \mathrm{px}^2$) with the object-to-image plane mapping function [32] determined with a precision-machined, dual-plane calibration target. Misalignment of the target with the laser sheet is corrected with the disparity map method [32–34] for which 20 images (of the undisturbed freestream) were used. Here 985 image pairs were taken at 1000 Hz (0.985 sec of acquisition time) for streamwise velocity field measurements where the laser pulse delay was 100,70, and 30 μs for the $\mathcal{R} = 0.75/1$, 1.5, and 3 wings, respectively. For cross-stream velocity field measurements, 500 image pairs were acquired at a frequency of 500 Hz (1 sec acquisition time). A concern for the cross-flow PIV measurements is the large through-plane component of velocity that can result in lost particle pairs due to out-of-plane motion. To mitigate this, the laser pulse delay was set to be 80,70, and 35 μs for the cross-flow measurements of the $\mathcal{R} = 0.75/1$, 1.5, and 3 wings, respectively, which limited the maximum particle displacement through the laser plane (using the freestream velocity as the through-plane velocity component) to be less than 20% of the laser sheet thickness for all cases.

The images are processed with Insight 4G software by TSI Inc. First, the images are dewarped according to calibration images taken for each camera. Thereafter, an iterative multipass DPIV evaluation algorithm consisting of windowing shifting or deformation was performed on each image pair. For both cross-stream and streamwise measurements the interrogation windows are made rectangular starting from a $64 \times 64\ \mathrm{px}^2$ down to $32 \times 32\ \mathrm{px}^2$ with 50% overlap. The spatial resolutions of the cross-flow measurements for each wing in the horizontal and vertical directions are $\Delta y = \Delta z = 0.0495c$, $0.0594c$, and $0.119c$ for the $\mathcal{R} = 0.75/1$, 1.5, and 3 wings, respectively. The spatial resolutions of the streamwise flow measurements for each wing in the horizontal and vertical directions are $\Delta x = \Delta z = 0.0313c$, $0.0376c$, and $0.0751c$ for the $\mathcal{R} = 0.75/1$, 1.5, and 3 wings, respectively.

B. Error analysis and methods

Statistics of undisturbed freestream measurements are used to quantify experimental errors in both cross-stream and streamwise velocity measurements. Time-averaging the in-plane velocity fields yielded spatial errors in the measurement field of view to be less than 5% of the freestream. Vorticity was calculated from in-plane velocity fields by the local circulation method [35]; error in vorticity, assuming uncorrelated velocity data, is therefore $e_\omega = 0.61 e_U/\Delta x = 0.94$, 0.76, and 0.20 for the $\mathcal{R} = 0.75/1$, 1.5, 3 wings where e_U is taken as the 2σ in-plane velocity error. Vorticity stemming from the two 6.35 mm diameter mounting rods (mounted on the pressure side of the wing) did introduce vorticity into the flow which was measured above the e_ω. This vorticity was well isolated from the free vorticity originating from the wing and was neglected when computing circulation. No other corrections were made to take into account the influence of the mount.

The tip vortices are identified by their strength and core location. The circulation of each tip vortex was computed by the area integral of vorticity in the core where the vorticity was thresholded above e_ω. The γ_1 criteria [36] was used to locate the core center locations for each test case. γ_1 is a scalar function defined at P as

$$\gamma_1(P) = \frac{1}{N}\sum_s \frac{(\boldsymbol{PM} \wedge \boldsymbol{U_M})\cdot \boldsymbol{z}}{||\boldsymbol{PM}||\cdot||\boldsymbol{U_M}||} = \frac{1}{N}\sum_s \sin(\theta_M), \tag{1}$$

where S is a two-dimensional area surrounding P, M lies in S, $\boldsymbol{z}$ is the unit vector normal to S, and N is the number of points M inside S. Here θ_M represents the angle between the velocity vector $\boldsymbol{U_M}$ and the radius vector $\boldsymbol{PM}$. $|\gamma_1|$ is bounded by 1 where high magnitudes of γ_1 mark regions of high swirl. The center of the vortex is determined by local maximum detection of the γ_1 field.

The time-averaged cross-stream velocity field is used to compute properties of the tip vortex. The averaging process is not modified to account for core wandering. However, to give a sense of the effects of core wandering, statistics of the instantaneous vortex properties were calculated for the Æ $= 1$ wing at all angles of attack for the zero sideslip case. We include the root-mean-square (RMS) error of the time series of instantaneous vortex properties as error bars for the Æ $= 1$ wing when the average tip vortex properties at zero sideslip are presented later in the paper. The RMS velocity fluctuations at the core center was measured to be less than 15% of the freestream at all angles of attack.

III. ANALYSIS

Measurements at zero sideslip, $\beta = 0^\circ$, are first analyzed to identify spanwise nonuniformities that may result in potential asymmetries for the wing in sideslip. Thereafter, measurements at $\beta = -10^\circ$ are discussed.

A. Measurements at $\beta = 0^\circ$

Topological changes of the tip vortex with increasing angle of attack are first discussed. Figure 4 plots characteristic vortex parameters at the trailing edge of the wing as a function of angle of attack and wing aspect ratio at zero sideslip $\beta = 0^\circ$. The quantities $\Gamma/(bU_\infty)$, d_c/b, and z_c/c correspond to nondimensional circulation, horizontal spacing, and vertical height of the vortex pair, respectively, where b is the span, c is the chord, and U_∞ is the freestream velocity. Also plotted in Fig. 4 are the tip vortex circulation and vertical core location measured by Kaplan *et al.* [37] on a thin, blunt-edged, Æ $= 2$ rectangular wing at a distance 0.1c downstream of its trailing edge at $\mathrm{Re}_c = 24{,}083$.

In terms of how the tip vortex pair evolves with increasing angle of attack for the Æ $\leqslant 1$ wings, the tip vortices grow in strength [Fig. 4(a)] with the core centers drawing closer together [Fig. 4(b)] as they collectively lift off the wing [Fig. 4(c)]. Note that the vortex properties of the Æ $= 1.5$ and 3 wings are not included at the tested angles of attack $\alpha > 10^\circ$ in Fig. 4 as stalled flow was evinced in the measured flow fields at these angles of attack.

Figure 5 plots time-averaged spanwise vorticity contours computed from streamwise velocity field measurements as a function of angle of attack. The surface of the wing is marked by a black line at the spanwise location at which the vorticity was computed. The insets are contour plots of time-averaged streamwise vorticity in the cross-flow plane at the trailing edge of the wing. Lift curves of each wing are also provided for reference in Fig. 5(a), where lift coefficient, C_L, is scaled by Helmbold's theoretical lift curve slope for flat-plate low-aspect-ratio straight wings [38], $C_{L_\alpha} = 2\pi/(\sqrt{1 + (2/AR)^2} + 2/AR)$. The theoretical curve for this inviscid flow theory is plotted as a black line.

Figure 6 complements Fig. 5 with measurements of the circulation distribution associated with positive and negative time-averaged spanwise vorticity in each measurement plane as a function of angle of attack. The circulation was calculated as the discrete area integral of the unfiltered vorticity field thresholded to isolate the positive and negative vorticity in the flow. The circulation associated with positive spanwise vorticity, represented as Γ_y^+, stems from bound vorticity of the wing

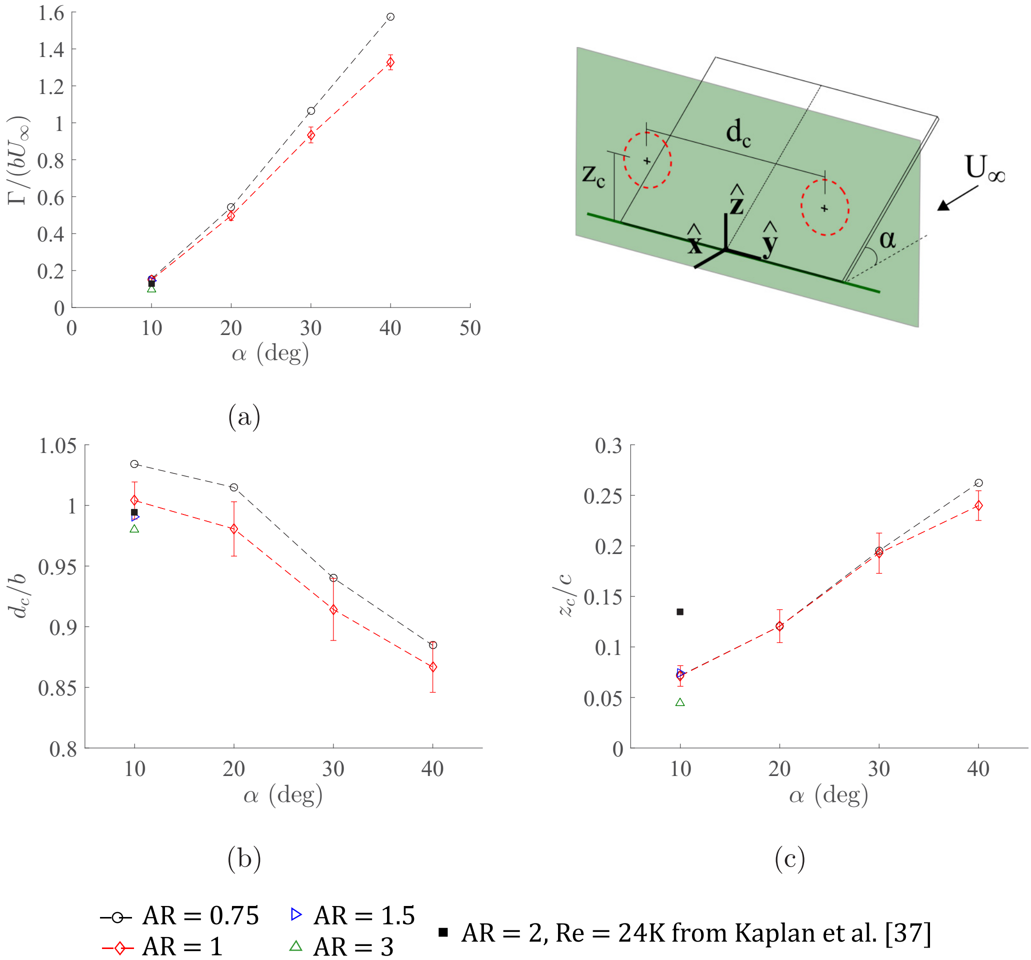

(a)

(b)

(c)

FIG. 4. Tip vortex (a) circulation, (b) horizontal spacing, and (c) vertical location each as a function angle of attack and wing aspect ratio, $\beta = 0^\circ$. The measurement plane is at the trailing edge of the wing and is orientated normal to the freestream. The root-mean-square error of the instantaneous vortex parameters is plotted as error bars for the Æ $= 1$ wing. The vortex properties are not plotted for cases where stalled flow is evinced in the measurement plane.

and the leading-edge vorticity. The circulation associated with trailing-edge vorticity, of opposite sign, is represented as Γ_y^-. A surface plot is superimposed to help resolve low magnitudes of Γ_y^-. Taken together, measurements of Γ_y^+ and Γ_y^- give indication of the "effective bound circulation" [21] distribution of the wing. At certain angles of attack the leading-edge vorticity could not be distinguished from the vorticity stemming from the core of the tip vortex, and thus Γ_y^+ and Γ_y^- are not plotted in Fig. 6 for those cases. In addition, the camera perspective for the streamwise measurements of the wings at zero sideslip disallowed the recovery of velocity vectors immediately downstream of the right wing's trailing edge. In order to appropriately compare the strength of trailing-edge vorticity across the span of the wing, Γ_y^- was computed at in-plane locations containing vorticity vectors common to all measurement planes for the given wing. Therefore, while the Γ_y^- measurements in Fig. 6 underpredict the true magnitude of Γ_y^-, they nonetheless accurately portray the trends in Γ_y^- with angle of attack and spanwise location. This perspective error and consequent underprediction of Γ_y^- did not occur for the measurements in sideslip.

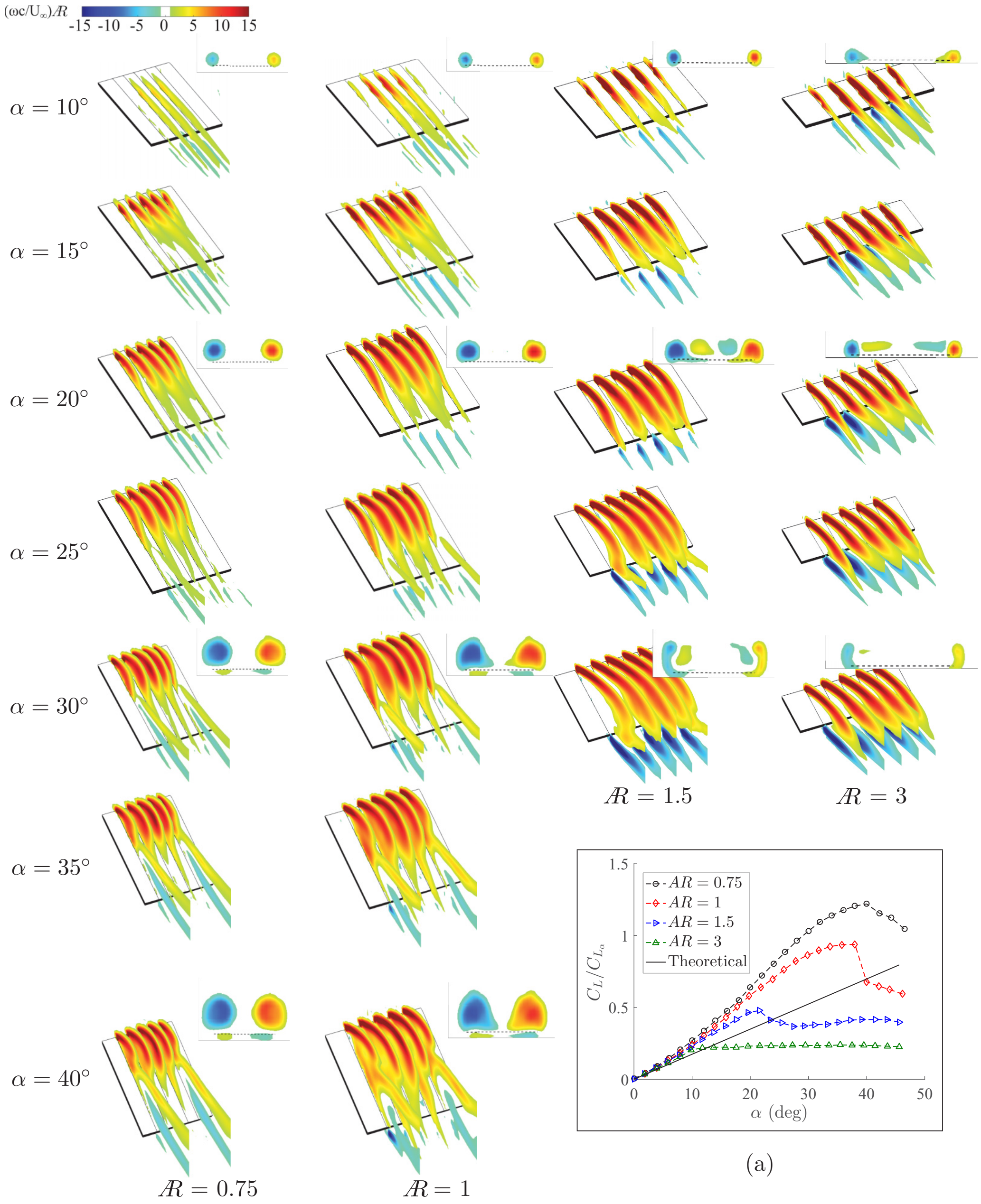

FIG. 5. Time-averaged spanwise vorticity contours as a function of angle of attack, $\beta = 0^\circ$. (Insets) Time-averaged streamwise vorticity at the trailing edge in a plane normal to freestream. (a) Lift ratio, C_L/C_{L_α}, as a function of angle of attack. C_{L_α} is Helmbold's theoretical lift curve slope [38].

We start by considering the time-averaged spanwise vorticity contours at the midplane, $y/b = 0$, of the $\mathcal{R} = 0.75$, 1, and 1.5 wings in Fig. 5 alongside the corresponding circulation measurements of Fig. 6. The positive spanwise vorticity near the midspan, while initially attached and parallel to the chord at $\alpha = 10^\circ$, is lifted off of the wing at $\alpha = 15^\circ$ and aligned more closely with the freestream.

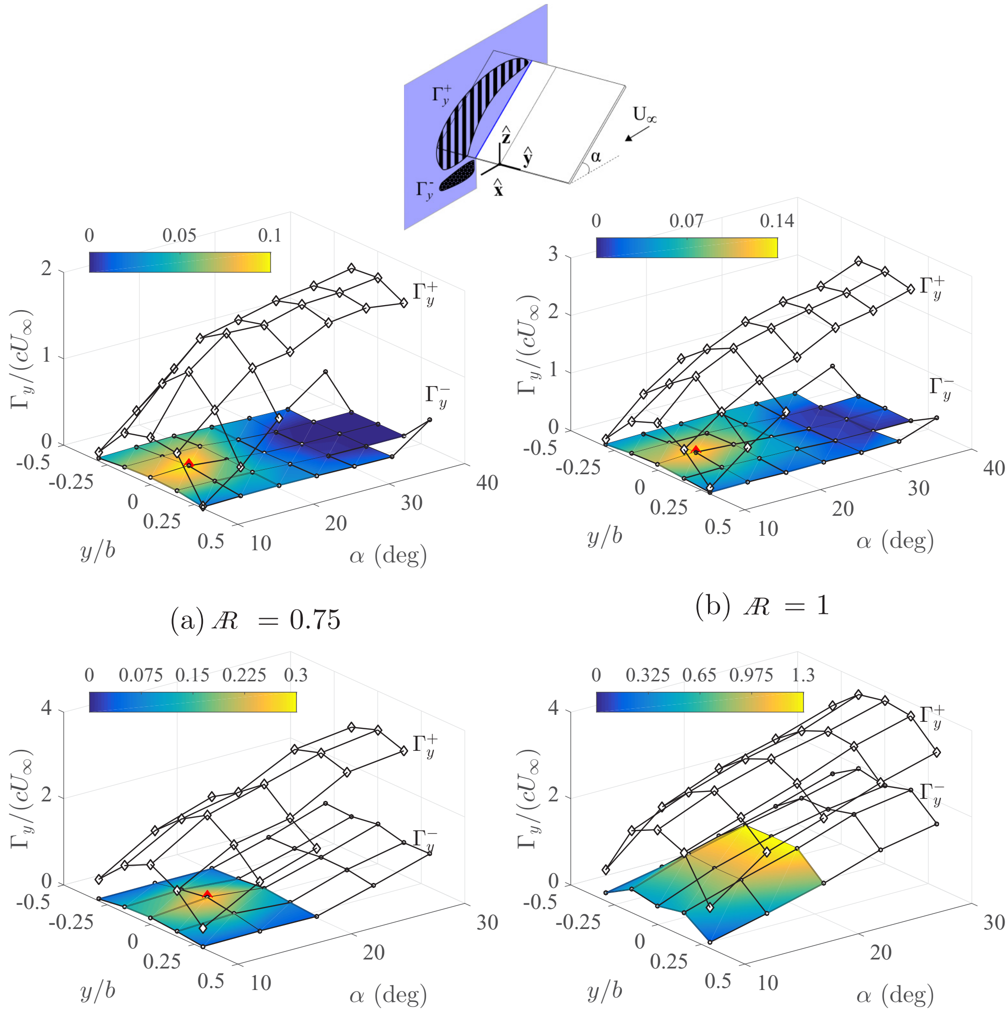

(a) $\mathit{A\!R} = 0.75$

(b) $\mathit{A\!R} = 1$

(c) $\mathit{A\!R} = 1.5$

(d) $\mathit{A\!R} = 3$

FIG. 6. Circulation associated with time-averaged positive and negative spanwise vorticity, Γ_y^+ and Γ_y^-, as a function of spanwise location and angle of attack for (a)–(d) $\mathit{A\!R} = 0.75$–3 rectangular wings at $\beta = 0°$. A surface plot is superimposed to highlight low magnitudes of Γ_y^-. Red markers indicate local maxima.

This is followed by a steep increase in Γ_y^+ and subsequent increase in Γ_y^- [Figs. 6(a)–6(c)]. Here, higher magnitudes of positive and negative vorticity are measured at the midspan of the wing. The red marker in Fig. 6 highlights a local maximum in Γ_y^- which occurs at the midspan. Trailing-edge vorticity of reduced magnitude occurs in chordwise planes closer toward the wing tips and at angles of attack immediately above and below $\alpha = 15°$. It will be shown later that the origin of high magnitude time-averaged trailing-edge vorticity stems from leading-edge vortex shedding at this angle of attack.

At increased angle of attack, $\alpha = 20°$ for the $\mathit{A\!R} = 0.75$, 1, and 1.5 wings, the vorticity contours at the midspan of the wing show the leading-edge vorticity curved back toward the wing surface near the trailing edge (Fig. 5). At this angle of attack, the strength of trailing-edge vorticity, Γ_y^-, decreases while Γ_y^+ continues to increase [Figs. 6(a)–6(c)]. For spanwise stations outboard of the midspan and closer to the wing tips, the leading-edge vorticity concentrates closer to the wing (Fig. 5) with strength of trailing-edge vorticity reduced [Figs. 6(a)–6(c)]. The lift produced by the $\mathcal{R} = 1.5$ wing is at its maximum at $\alpha = 20^\circ$ and has stalled by $\alpha = 25^\circ$ as shown in Fig. 5(a). At $\alpha = 25^\circ$, leading-edge vorticity at the three innermost streamwise slices is no longer reattached to the wing surface. Concurrently, a steep increase in trailing-edge vorticity is measured, Γ_y^- [Fig. 6(c)]. In contrast, the leading-edge vorticity of the $\mathcal{R} = 0.75$ and 1 wings at $\alpha \geqslant 25^\circ$ remains pinned back to the wing and is no longer organized in a layer as was seen at $\alpha = 10$–20° but is clustered into a hemispherical shape on the wing. In addition, from $\alpha = 25$–35° the strength of trailing-edge vorticity remains of low magnitude and is more uniform across the trailing edge of the wing than at the lower tested angles of attack in the range $\alpha = 10$–20°, Figs. 6(a) and 6(b).

Throughout the tested angle of attack range for the $\mathcal{R} = 0.75$ and 1 wings, the tip vortices grow in size and migrate inboard as they lift off the wing (Fig. 5) with increasing angle of attack. At high angles of attack starting around $\alpha = 25^\circ$, the total lift of the $\mathcal{R} = 0.75$ and 1 wings begin to taper off, Fig. 5(a), with the angle of attack of maximum lift occurring in the range $\alpha \approx 35$–40°. In this angle of attack range, opposite-signed spanwise trailing-edge vorticity is measured toward the wing tips, specifically under the cores of the tip vortex [Figs. 5, 6(a), and 6(b)]. In addition, streamwise vorticity of opposite sign is measured underneath the tip vortex beginning at $\alpha = 30^\circ$. Collectively, such measurements indicate the tapering off of total lift at high angles of attack is due in part to the lift off of the tip vortex and the subsequent stall of flow directly beneath it.

The $\mathcal{R} = 3$ wing experiences more advanced stages of separated flow at a given angle of attack. Beginning at $\alpha = 10^\circ$ the boundary layer separates from the wing in the form of a shear layer that continues to remain detached from the wing with increasing angle of attack. The sustained detachment of the leading-edge shear layer is complemented with increased vorticity generation at the trailing edge, Γ_y^- [Fig. 6(d)]. At $\alpha > 10^\circ$, Γ_y^+ and Γ_y^- increase at the same rate across the span of the wing. From Joukowski's lift formula, $L(y) = \rho U_\infty[\Gamma_y^+(y) - \Gamma_y^-(y)]$, lift must remain constant at such poststall angles of attack for the $\mathcal{R} = 3$ wing. This is indeed consistent with force measurements in Fig. 5(a).

Analysis of the unsteady flow field in both cross-stream and streamwise measurement planes provides additional insight into the connection between the organization of leading-edge vorticity and the appearance of opposite-signed trailing-edge vorticity. Figure 7 plots the turbulence kinetic energy (TKE) with superimposed time-averaged velocity vectors in cross-flow planes at the wing's trailing edge at zero sideslip, $\beta = 0^\circ$. The additional scaling by $\mathcal{R}$ for the nondimensional TKE is employed to align the peak TKE values across the $\mathcal{R} \leqslant 1.5$ wings enabling the use of a single scale. A projection of the wing's trailing edge on the measurement plane is also depicted for reference. Blue dots are used to mark the cross-stream location of the streamwise measurement planes for comparison purposes.

At all tested angles of attack for wings experiencing increased lift, the spatial region with the largest TKE levels between the vortex cores, dark regions shown in Fig. 7, occurs at the midspan where "more steady" flow regions, as evinced by lower levels of TKE, occur toward the wing tips. By $\alpha = 20^\circ$ evidence of separated flow exists at the trailing-edge of the $\mathcal{R} \geqslant 1.5$ wings by inspection of the magnitude of time-averaged in-plane velocity. The spanwise locations of stalled flow in the cross-flow plane coincides with the complete detachment of leading-edge vorticity from the wing and the discharge of strong trailing-edge vorticity from the wing's trailing edge, as measured in Fig. 5 and Figs. 6(c)–6(d), respectively.

For the $\mathcal{R} \leqslant 1.5$ wings, the TKE at the trailing-edge intensifies from $\alpha = 10^\circ$ to $\alpha = 20^\circ$. However, the flow in the time-averaged sense is nowhere stalled at the trailing edge of the $\mathcal{R} = 0.75$ and 1 wings as was measured for the higher $\mathcal{R}$ wings. Analysis of movies of the instantaneous spanwise vorticity at $\alpha = 20^\circ$ highlight the highly unsteady and transitional nature of the leading-edge shear layer at this angle of attack. The leading-edge shear layer breaks up and sheds vorticity downstream into the wake. The vorticity that is shed is multiscaled and has varying convective

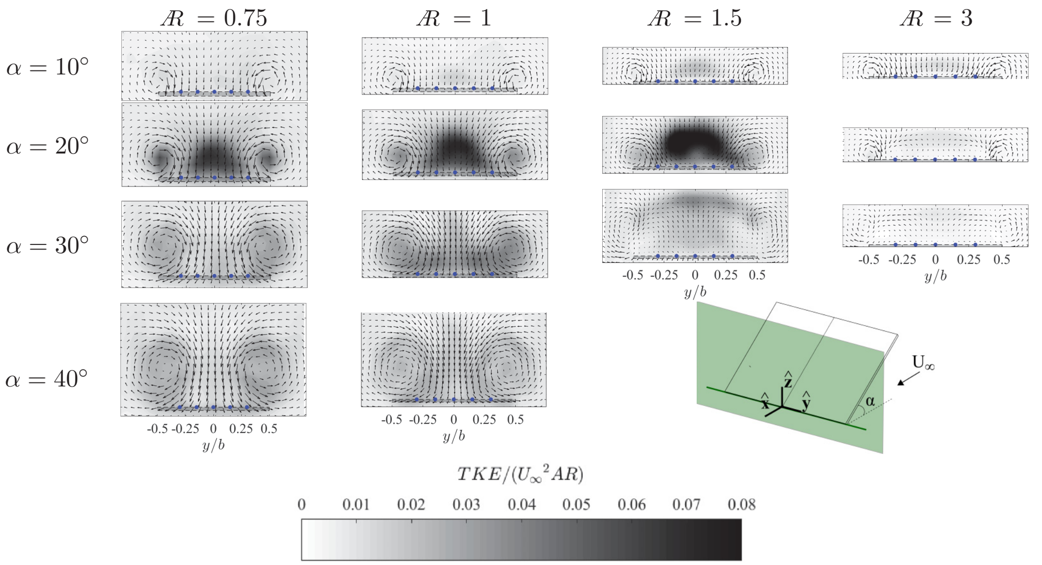

FIG. 7. TKE with superimposed time-averaged velocity vectors in a measurement plane orientated normal to the freestream at a streamwise distance coincident with the trailing edge of inclined rectangular flat plate wings of various aspect ratio, $\beta = 0°$. Blue dots mark the spanwise location at which streamwise flow-field measurements were taken.

velocities. Figure 8 shows representative snapshots of instantaneous spanwise vorticity that depict a shedding cycle of large-scale leading-edge vorticity on the $Æ = 1$ wing at $\alpha = 20°$ at spanwise locations $y/b = 0$ (midspan), $y/b = 0.15$, and $y/b = 0.30$. The nondimensional period of the shedding cycle at $y/b = 0$ is $T^* = TU_\infty/c = 2.13$. Note that the time series of measurements at

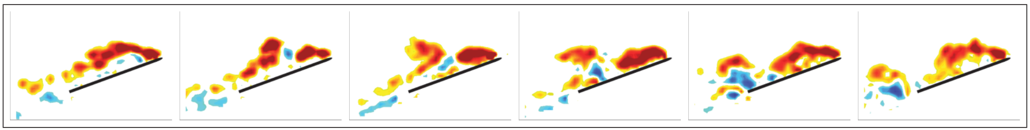

(a) $y/b = 0$

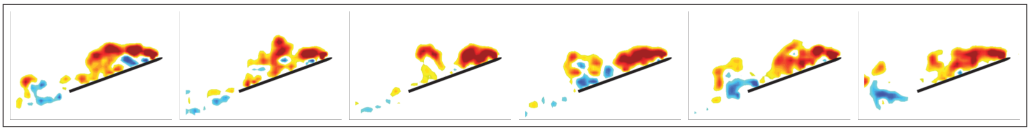

(b) $y/b = 0.15$

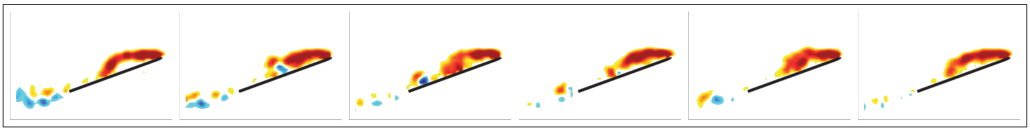

(c) $y/b = 0.30$

FIG. 8. Snapshots of instantaneous vorticity at (a) $y/b = 0$, (b) $y/b = 0.15$, and (c) $y/b = 0.30$ on an $Æ = 1$ wing at $\alpha = 20°$ at zero sideslip. y/b is measured with respect to the midspan of the wing. The time between snapshots is $t^* = T^*/6$ where $T^* = TU_\infty/c = 2.13$ is the nondimensional shedding period at $y/b = 0$.

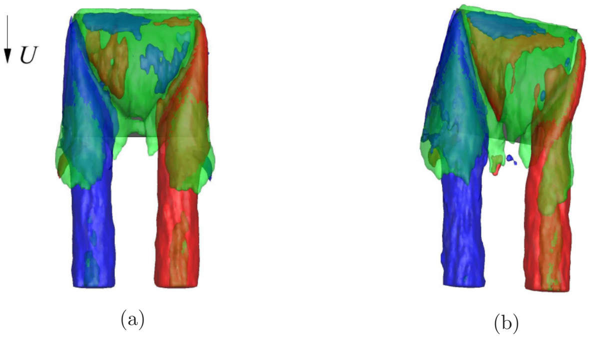

(a) (b)

FIG. 9. Vorticity isosurfaces of $Æ = 1$ wing at (a) $\beta = 0^\circ$ and (b) $\beta = -10^\circ, \alpha = 35^\circ$. Replotted from DeVoria and Mohseni [25]. The spanwise- and streamwise-orientated vortex structures are marked green and red/blue, respectively.

different spanwise locations are not synchronized in time with each other. At the spanwise locations near and at the midspan, $y/b = 0.15$ and $y/b = 0$, large-scale clusters of strong positive vorticity, initially shed from the leading-edge shear layer, pair up with opposite-signed vorticity on the wing and collectively traverse the chord of the wing into the wake. Toward the wing's side edge, $y/b = 0.30$, the vorticity comprising the leading-edge shear layer curves back to the wing with less deviation from this configuration. A similar pairing and shedding of opposite-signed vorticity clusters occurs; however, in contrast, the shed vorticity is of much smaller scale and traverses the wing close to the wings surface with a faster convection velocity.

Returning to Fig. 7, the magnitude of the TKE is less at the midspan at $\alpha = 30^\circ$ and $\alpha = 40^\circ$ than at the lower angle of attack, $\alpha = 20^\circ$. Movies of the instantaneous vorticity at these higher angles of attack show the majority of leading-edge vorticity recirculating above the wing as opposed to shedding downstream into the wake. This is consistent with the time-averaged vorticity measurements (Fig. 5), where the leading-edge vorticity is clustered atop the wing. The decrease in leading-edge vorticity shed passed the trailing edge reduces the average discharge of opposite-signed vorticity there; recall the time-averaged measurements of the strength of trailing-edge vorticity, Γ_y^-, in Fig. 6. In this angle of attack regime, the downwash of the tip vortex is sufficient to reduce the downstream shedding of leading-edge vorticity into the wake enabling a more steady matching of flow at the trailing edge. Such action sustains the lift-generating ability of the leading-edge separation region at high angles of attack. Ultimately, both the ability of the tip vortex downwash to restrict vortex shedding at high angles of attack and the lift off of the tip vortex will be key points of similarity with measurements in sideslip, having notable consequences regarding the lateral stability of the wing.

B. Measurements at $\beta = -10^\circ$

The time-averaged three-dimensional vortex structure of a $Æ = 1$ wing at $\alpha = 35^\circ$ at both zero and nonzero sideslip has been measured by DeVoria and Mohseni [25]. Top views of the vortex structures at $\beta = 0^\circ$ and $\beta = -10^\circ$ are replotted in Figs. 9(a) and 9(b), respectively, for visual reference. The spanwise-orientated vortex sheet stemming from the leading edge is marked green and is translucent to show the vortex structures underneath. The streamwise-orientated vortex structures that are not enveloped in the leading-edge vortex sheet correspond to the left (windward) and right (leeward) tip vortices and are marked blue and red, respectively, for the wing at $\beta = 0^\circ$ ($\beta = -10^\circ$). At $\beta = -10^\circ$ the windward tip vortex of the $Æ = 1$ wing convects nearly parallel to the freestream throughout its downstream evolution, whereas the leeward tip vortex "hugs" the leeward wing edge and then reorientates itself parallel to the freestream upon passing the trailing edge of the wing. This contrasts with the $\beta = 0^\circ$ case where the left and right tip vortex are symmetric about the midspan of the wing and both evolve parallel to the freestream in this top view. The circulation of

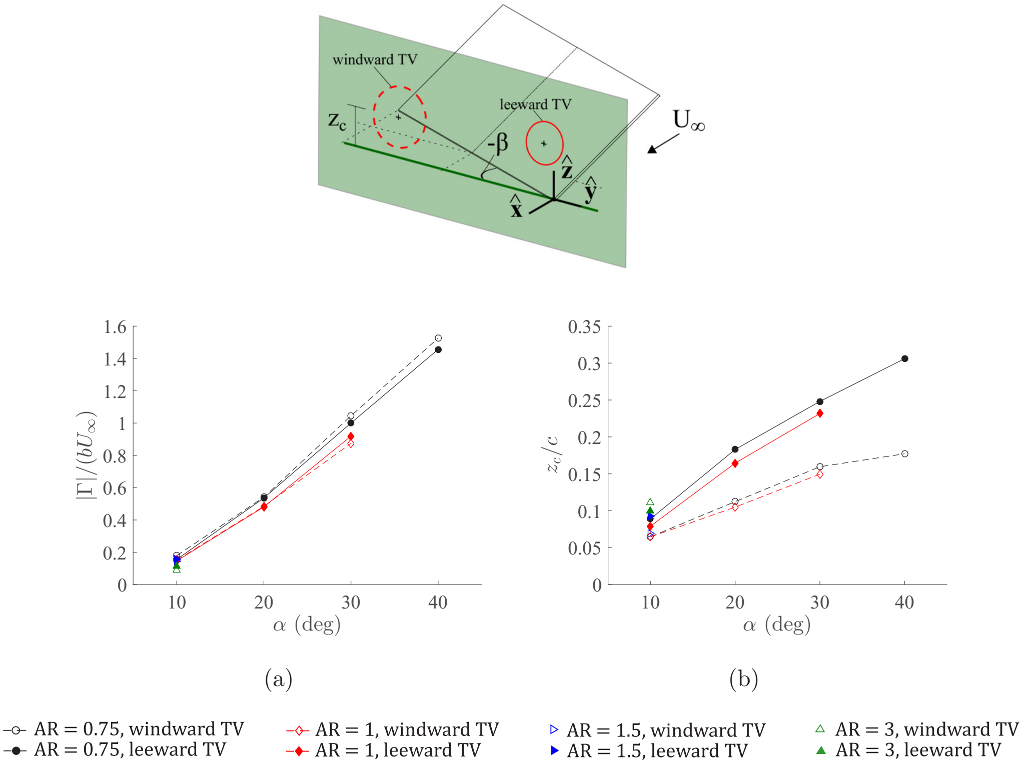

(a)

(b)

FIG. 10. Tip vortex (a) circulation and (b) vertical location as a function angle of attack and wing aspect ratio, $\beta = -10^\circ$. The measurement plane is orientated normal to the freestream at a streamwise distance coincident with the leeward trailing corner. The vortex properties are not plotted for cases where stalled flow is evinced in the measurement plane.

both tip vortices at $\beta = -10^\circ$ increase with downstream distance eventually reaching a nominally constant, near equivalent value upon passing the furthest downstream point of the respective side edge [25].

As in the zero sideslip case, we start by analyzing the characteristics of the tip vortex at the trailing edge as angle of attack is increased for the wing at $\beta = -10^\circ$. Figure 10 plots properties of the windward and leeward tip vortex. The vortex properties of the $\mathcal{R} = 1.5$ and 3 wing at $\alpha > 10^\circ$ and the $\mathcal{R} = 1$ wing at $\alpha = 40^\circ$ are not plotted due to the measurement of stalled flow at the trailing edge. As the circulation of both tip vortices is nearly equivalent at the tested angles of attack [Fig. 10(a)], the main effect of sideslip is to introduce spatial asymmetries in the tip vortex structures. From Fig. 10(b), the leeward tip vortex is located higher above the wing than the windward tip vortex at all tested angles of attack. Moreover, the height of the leeward tip vortex increases at a faster rate with angle of attack than the leeward vortex. Based on this orientation of the vortex pair with increasing angle of attack, the resultant lift of the tip vortex system would favor an increasingly restorative roll moment in sideslip (i.e., positive roll moment in this negative sideslip configuration).

Following the same analysis procedure as the zero sideslip case, Fig. 11 plots time-averaged vorticity contours computed from streamwise velocity field measurements as a function of angle of attack. As the measurement plane is parallel to the freestream, the in-plane vorticity for the sideslip case is not spanwise but cross-stream vorticity. A dashed line is also plotted on each figure to represent what would be the trailing edge of the wing at zero sideslip. The insets depict streamwise vorticity at a measurement plane orthogonal to the freestream and coincident with this dashed line.

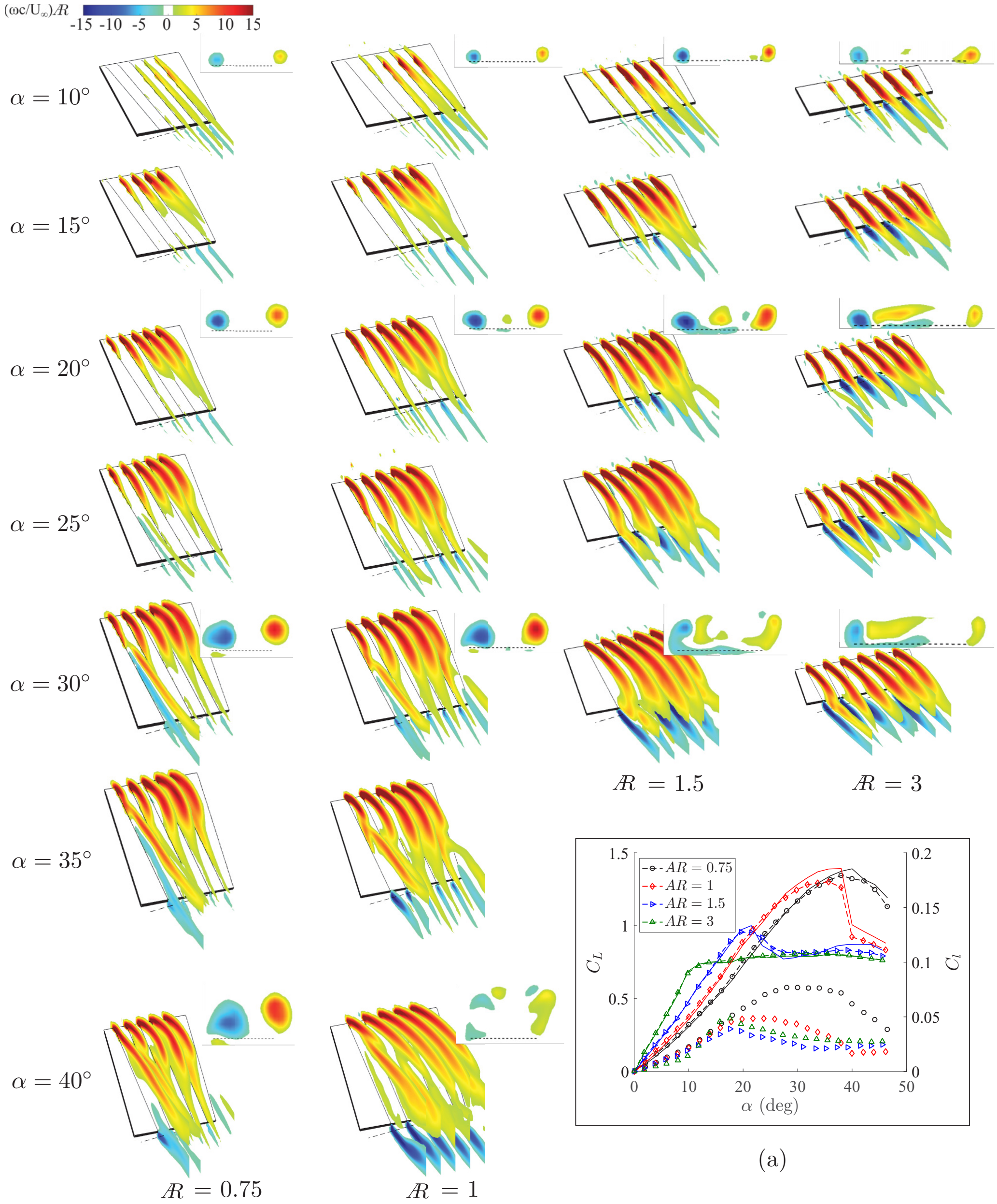

FIG. 11. Time-averaged cross-stream vorticity contours as a function of angle of attack, $\beta = -10°$. (Insets) Time-averaged streamwise vorticity in a plane normal to freestream at streamwise location marked by the dotted line. (a) Lift (dashed markers), C_L, and roll moment (markers only), C_l, versus angle of attack, $\beta = -10°$. C_L at $\beta = 0°$ (solid line).

Coefficient of lift, C_L, and roll moment, C_l, curves for each wing at $\beta = -10°$ are also provided for reference in Fig. 11(a). The corresponding lift curves of each wing at zero sideslip, $\beta = 0°$, are also plotted and serve to display the similarity in lift generation between the two sideslip angles.

In conjunction with the time-averaged vorticity contours of Fig. 11, Fig. 12 displays measurements of Γ_y^+ and Γ_y^-. At certain angles of attack the leading-edge and trailing-edge vorticity could not be

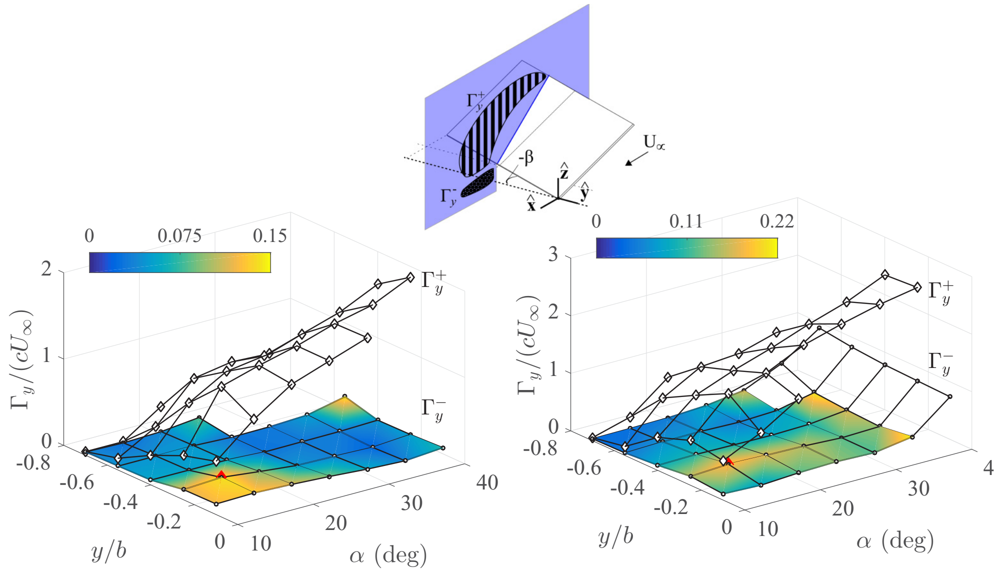

(a) $\mathit{AR} = 0.75$ (b) $\mathit{AR} = 1$

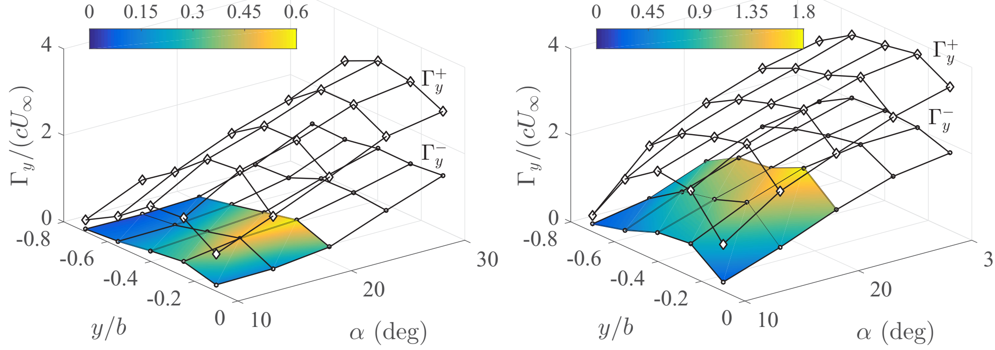

(c) $\mathit{AR} = 1.5$ (d) $\mathit{AR} = 3$

FIG. 12. Circulation associated with time-averaged positive and negative cross-stream vorticity, Γ_y^+ and Γ_y^-, as a function of cross-stream location and angle of attack for (a)–(d) $\mathit{AR} = 0.75$–3 rectangular wings at $\beta = -10^\circ$. A surface plot is superimposed to highlight low magnitudes of Γ_y^-. Red markers indicate local maxima.

distinguished from the cross-stream vorticity in the core of the tip vortex. Measurements of Γ_y^+ and Γ_y^- are excluded in Fig. 12 for those cases.

We start by addressing the symmetry of the time-averaged vorticity field as angle of attack is increased. At low angles of attack, $\alpha \leqslant 20^\circ$, the cross-stream vorticity is asymmetric about the midspan of the sideslipped wing as higher magnitudes of both positive and negative vorticity is measured on the leeward portion of the wing (Figs. 11 and 12) with more attached flow existing on the windward wing. We suspect such asymmetry to be attributed in part due to the transport of leading-edge vorticity toward the leeward portion of the wing, encouraged by the introduction of spanwise flow for this sideslipped configuration.

At $\alpha > 15^\circ$, the leading-edge vorticity curves back toward the wing for the $\mathit{AR} = 0.75$ and 1 wings, similar to the zero sideslip case. With increased angle of attack the strength of trailing-edge

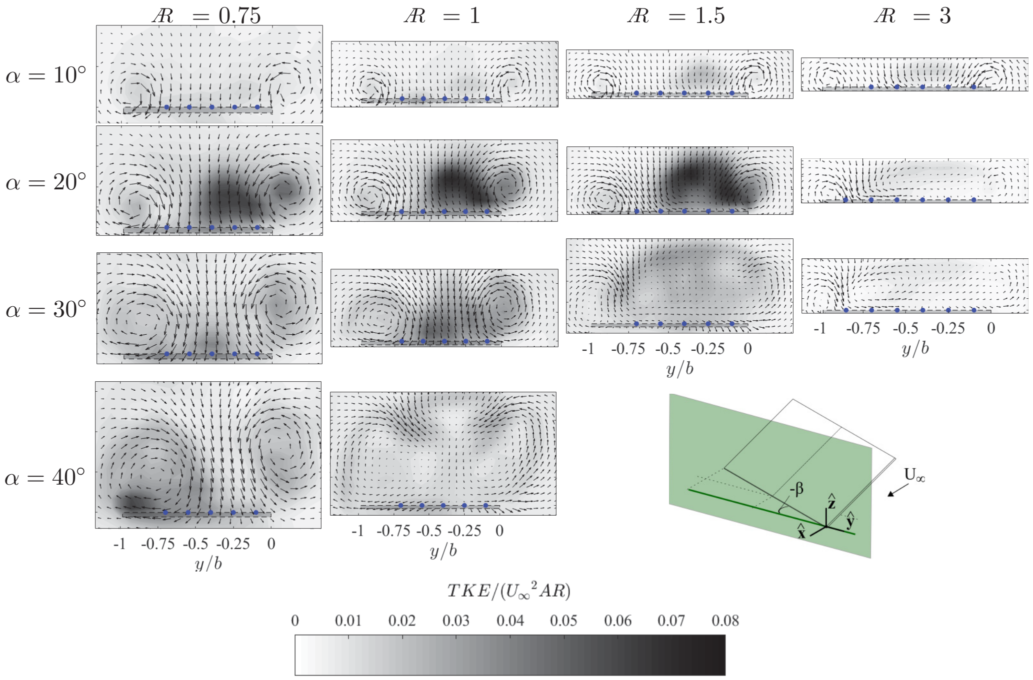

FIG. 13. TKE with superimposed time-averaged velocity vectors in a measurement plane orientated normal to the freestream at a streamwise distance coincident with the leeward trailing edge of inclined rectangular flat plate wings of various aspect ratio in sideslip, $\beta = -10°$. Blue dots mark the spanwise location at which streamwise flow-field measurements were taken.

vorticity, Γ_y^-, decreases on the leeward wing [Figs. 12(a) and 12(b)] signaling the sustained lift of the leading-edge separation region at high angles of attack in sideslip. Simultaneously, the windward tip vortex grows in size with its vorticity distribution increasingly more diffuse as angle of attack increases (inset figures of Fig. 11). With its spatial growth, the windward tip vortex occupies an increasingly larger percentage of the windward wing further displacing the leading-edge separation region toward the leeward wing. Simultaneously, the leeward tip vortex lifts off the wing while elongating in the vertical direction.

Similar to the zero sideslip case, preliminary signs of lift loss are measured for the $\mathcal{R} = 1$ and 0.75 wings beginning around $\alpha = 25°$ by the appearance of cross-stream trailing-edge vorticity under the windward tip vortex core (Fig. 11). In addition, at $\alpha = 30°$, opposite-signed streamwise vorticity is measured under the windward core. With increasing angles of attack, the strength of trailing-edge vorticity on the windward wing sharply increases relative to that which is measured in cross-stream measurement planes toward the leeward wing [Fig. 12(b)]. By $\alpha = 40°$, high-magnitude trailing-edge vorticity fully spans the $\mathcal{R} = 1$ wing with the coherency of the tip vortices extinguished at the trailing edge, altogether signaling the acute loss of lift.

For the $\mathcal{R} = 3$ wing fully separated flow initiates on the leeward wing and rapidly evolves upstream toward the windward wing with increasing angle of attack (Fig. 11). It is clear that this evolution of stalled flow on the $\mathcal{R} = 3$ wing results in the distinct increase in roll moment beginning at the angle of attack of lift stall, $\alpha = 10°$, and the distinct reduction of roll moment at the angle of attack for which stalled flow has expanded past the midspan, $\alpha \approx 18°$.

The unsteady streamwise and cross-stream flow field is now analyzed to corroborate the origin of trailing-edge vorticity generation on the sideslipped wing. Figure 13 plots the TKE at the trailing

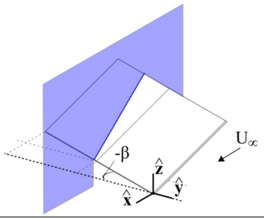

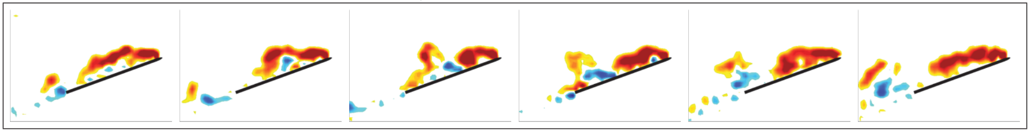
(a) $y/b = -0.25$

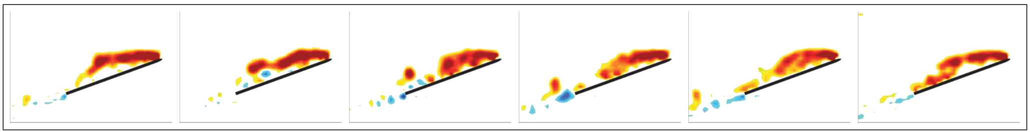
(b) $y/b = -0.55$

FIG. 14. Snapshots of instantaneous vorticity at (a) $y/b = -0.25$ and (b) $y/b = -0.55$ on an $A\!\!\!R = 1$ wing at $\alpha = 20^\circ$ at $\beta = -10^\circ$ with y/b measured with respect to the origin at the leeward trailing edge. The time between snapshots is $t^* = T^*/6$ where $T^* = TU_\infty/c = 2.13$ is the nondimensional shedding period at the midspan of the $A\!\!\!R = 1$ wing at $\alpha = 20^\circ$, $\beta = 0^\circ$.

edge of the sideslipped wing. Similar trends in the TKE versus angle of attack survive in sideslip on the tested wings; however, high-magnitude TKE regions at the trailing edge now reside toward the leeward wing. As angle of attack is increased from $\alpha = 10^\circ$ to $\alpha = 20^\circ$ the intensity and spanwise extent of the unsteady trailing-edge flow increases (Fig. 13). Stalled flow initiates on the leeward wing at $\alpha = 20^\circ$ for the $A\!\!\!R = 1.5$ and 3 wings by inspection of the magnitude of time-averaged velocity fields. With increasing angle of attack, the stalled flow region expands spatially toward the windward wing, as was measured to occur via cross-stream vorticity measurements of the separated region in Fig. 11.

Similar to the zero sideslip cases, the highest trailing-edge TKE levels at the tested angles of attack occur at $\alpha = 20^\circ$ for the $A\!\!\!R = 0.75$, 1, and 1.5 wings (Fig. 13). This is not unexpected as the lift curves of sideslipped LAR rectangular wings, $|\beta| < 10^\circ$, are nearly identical at these angles of attack; recall Fig. 11(a). As was done previously, we use representative snapshots of the instantaneous cross-stream vorticity fields to corroborate the origin of flow unsteadiness at the trailing edge. Figure 14 plots a time series of the instantaneous cross-stream vorticity field in streamwise planes located at $y/b = -0.25$ and $y/b = -0.55$ for the $A\!\!\!R = 1$ wing at $\alpha = 20^\circ$. The representative instantaneous cross-stream vorticity in the measurement plane on the leeward wing, $y/b = -0.25$, in Fig. 14(a), is similar in nature to that which is measured for the streamwise measurement planes at and near the midspan of the wings at zero sideslip at this angle of attack [recall Figs. 8(a) and 8(b)]; the leading-edge shear layer breaks up and sheds large-scale clusters of positive cross-stream vorticity which travel downstream pairing up with opposite-signed vorticity upon passing the trailing edge. At the streamwise measurement plane toward the windward portion of the wing, $y/b = -0.55$, the leading-edge shear layer is more steady, having less deviation from the seen configuration.

At higher angles of attack, $\alpha = 30^\circ$, a more steady uniform trailing-edge flow field is observed for the $A\!\!\!R = 0.75$ and 1 wings between the cores of the tip vortices as evinced by the reduction in the magnitude of TKE on the leeward wing (Fig. 13). Similar to the zero sideslip case at this angle of attack, analysis of movies of instantaneous cross-stream vorticity show the majority of leading-edge vorticity contained atop the wing as opposed to being shed downstream. The decrease in trailing-edge flow unsteadiness on the leeward wing decreases the magnitude of time-averaged

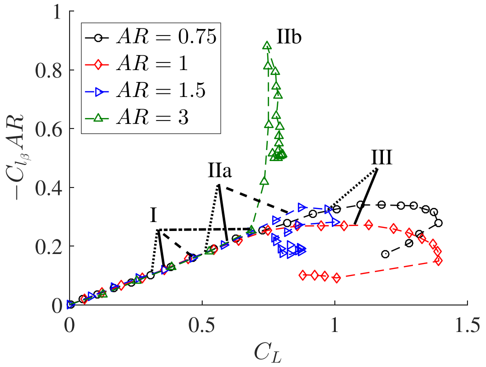

I: $\alpha \approx 10^\circ$, leading-edge separation.

IIa: $\alpha > 15^\circ$, downwash sufficient to curb the detachment of the leading-edge shear layer.

IIb: $\alpha = 18^\circ$, stalled flow region expands passed the midspan toward the windward wing.

III: $\alpha \approx 25^\circ$, tip vortex lift off.

FIG. 15. The negative of the product of lateral static stability derivative and wing aspect ratio, $-C_{l_\beta} AR$, versus the lift coefficient of the wing at zero sideslip, C_L. Roman numerals, I, IIa, IIb, and III, mark the approximate lift coefficients corresponding to specific angles of attack for the $AR = 0.75$ (dotted), 1 (solid), 1.5 (dashed), and 3 (dotted-dashed) wings.

trailing-edge vorticity (recall Fig. 12), sustaining the lift generating ability of the leading-edge separation region at high angle of attack.

IV. DISCUSSION

The previous analysis enables the following interpretation of the lateral static stability nonlinearities previously displayed in Fig. 1. We recall that lift is nearly independent of sideslip for small sideslip angles $|\beta| < 10^\circ$ [Fig. 11(a)]. Moreover, the relationship between roll moment and sideslip is nearly linear at each of the tested angles of attack [29]. Motivated by these observations, we expect the flow-field behavior to vary in a continuous manner as sideslip is incremented between the sideslip cases measured in this investigation, $\beta = -10^\circ$ and $\beta = 0^\circ$. The lateral stability curves of Fig. 1 are replotted here in Fig. 15 for ease of reference, and specific angles of attack are marked by Roman numerals.

At lift coefficients corresponding to $\alpha < 10^\circ$, the lateral static stability of the wing increases with lift due to the arrangement of bound vorticity on the sideslipped wing [24] and the nonlinear lift of the tip vortices. Roman numeral I marks the lift coefficients corresponding to $\alpha = 10^\circ$, which is the approximate angle of attack for which separation occurs at the leading edge of the wing as evinced by the streamwise vorticity measurements of Figs. 5 and 11. In this regime, additional lift stems the leading-edge separation region which emerges on the leeward wing in sideslip. Here both the lift and the lateral static stability of the $AR \leqslant 1.5$ wings continue to increase monotonically with subsequent increases in angle of attack initially after the formation of separation region, $\alpha \approx 10$–15°. In this approximate angle of attack range, leading-edge flow reattachment is highly unsteady as the tip vortices are of insufficient size and strength to restrict the downstream shedding of leading-edge vorticity.

For the $AR = 3$ wing the tip vortex downwash is insufficient to curb the complete detachment of the leading-edge shear layer. Stalled flow initiates on the leeward wing in sideslip, $\alpha = 10^\circ$, prompting a steep increase in stabilizing roll moment as the separated region expands to take up a larger portion of the leeward wing with subsequent increases in angle of attack. Eventually, at $\alpha = 18^\circ$ (Roman numeral IIb), the windward expansion of the fully separated-flow region crosses the midspan with its upstream evolution with angle of attack now reducing the lateral asymmetries associated with reattached or detached flow across the span. This prompts the sharp decrease in lateral stability at an angle of attack above lift stall (Fig. 15). This is roll stall for the $AR = 3$ wing.

For the $AR \leqslant 1.5$ wings, as angle of attack is increased past $\alpha \approx 15^\circ$ (lift coefficients marked by Roman numeral IIa), the downwash becomes sufficient to restrict leading-edge vortex shedding and more steadily reattach the leading-edge flow on the leeward portion of the wing. This sustains the lift-generating ability of the leading-edge separation region. Simultaneously, the windward tip vortex grows in size with increasing angle of attack causing it to occupy an increasing majority of the windward wing. The spatial growth of the windward core displaces the leading-edge separation region further toward the leeward wing. This reorganization of lift-generating-vorticity on the wing engages a competition between the lift of the separation region and that of the windward tip vortex that results in the initial decrease in the growth rate of lateral static stability at angles of attack of increasing lift. Inevitably, the lift of the $\mathcal{R} = 1.5$ wing stalls as the downwash is unable to maintain leading-edge flow reattachment. For the $\mathcal{R} = 0.75$ and 1 wings beginning at $\alpha = 25^\circ$, the windward tip vortex lifts off the wing resulting in the generation of opposite signed vorticity beneath it. The subsequent loss of sectional lift on the windward wing reduces the lateral stability of the wing at angles of attack near that of lift stall. This is roll stall for the $\mathcal{R} = 0.75$ and 1 wings.

While this investigation has focused on low-aspect-ratio wings with straight leading-edges, related trends in lateral static stability have been measured for wings with swept leading edges, which are worth mentioning. Stability reversal was measured on wings of 45° [39], 50° [40], and 60° [41] sweep at angles of attack prelift stall. Coe *et al.* [39] attributed the stability reversal to the emergence of fully separated flow on the windward portion of the sideslipped wing. This contrasts with the $\mathcal{R} = 3$ rectangular wing tested in this study where fully separated flow initiates on the leeward portion of the wing and results in the initial increase in lateral stability as opposed to stability reversal. A series of wings with 70° sweep was also tested [42]. Interestingly, the 70° swept wings did not exhibit full stability reversal but simply the reduction in lateral static stability at high angles of attack prelift stall. This lateral stability characteristic is similar to that of roll stall for the low-aspect-ratio rectangular wings ($\mathcal{R} \leqslant 1$) in this study. The results of these related studies indicate that the sweep angle may be yet another key geometric parameter of the wing that controls the roll stall characteristics of the wing.

Ultimately, the nonlinearities in lateral static stability associated with roll stall on LAR rectangular wings must be addressed either at the vehicle design or control level. A critical geometrical parameter that influences the nonlinear lateral stability characteristics is the wing aspect ratio. From Fig. 15, the lateral stability of the $\mathcal{R} = 0.75$ wing stays increasing to higher lift coefficients than the lower aspect-ratio wings. With further reduction in wing aspect ratio for the rectangular wing, we surmise that the angle of attack of roll stall would increase to eventually coincide with that of lift stall as the leading-edge separation region is lost and the free-vortex forces and moments become dominated by a single lifting mechanism, i.e., the tip vortices.

In addition to geometric modifications to the wing, flow control may also be used to modify the lateral stability characteristics at high angles of attack. For LAR wings that suffer from insufficient roll damping in the presence of strong stabilizing roll moments, passive measures such as wing-tip “bleed” [43] are encouraging in their ability to increase roll damping by manipulating the coherency of the tip vortex on the rolling wing without a substantial lift penalty in steady translating flight. It would be interesting to see the effects of wing-tip bleed on leading-edge flow reattachment in steady sideslip and the corresponding effects on C_{l_β}. Active flow control measures such as steady blowing [3] also show promise for directly influencing C_{l_β} in its ability to manipulate wake structures to modify the lift contribution of the separation region.

V. CONCLUDING REMARKS

In this investigation, stereoscopic digital particle image velocimetry was used to elucidate the fluid dynamics behind nonlinear trends between lateral static stability and lift at high angles of attack on various low-aspect-ratio (LAR) rectangular wings. At $\alpha = 10^\circ$, the leading-edge separation region emerges on the leeward wing in sideslip with flow reattachment a consequence of vortex shedding. From $\alpha = 10\text{–}15^\circ$, the downwash of the tip vortices is insufficient to steadily reattach the leading-edge flow on the leeward portion of the sideslipped wing. For the $\mathcal{R} = 3$ wing, intermittent flow separation quickly advances to fully separated flow on the leeward portion of the wing resulting in large stabilizing roll moments at subsequent increases in angle of attack above that of lift stall. At increasingly higher angles of attack for the $\mathcal{R} = 3$ wing, the stalled flow region grows in breadth expanding upstream on the wing. This reduces the lateral asymmetries associated with reattached or detached flow across the span which consequently reduces the stabilizing roll moment at an angle of attack above that of lift stall.

For the $\mathcal{R} \leqslant 1.5$ wings at $\alpha > 15^\circ$, the tip vortex downwash becomes sufficient to restrict the downstream shedding of leading-edge vorticity enabling the more steady reattachment of leading-edge flow on the leeward wing in sideslip. This action sustains the lift-generating ability of the leading-edge separation region to higher angles of attack for wings of decreasing aspect ratio. At increasing angles of attack for the $\mathcal{R} = 0.75$ and 1 wings, the windward tip vortex core grows in size and strength displacing the leading-edge separation region increasingly toward the leeward wing. We interpret such restructuring of lift-generating vorticity to result in the initial decrease in the growth rate of lateral static stability at angles of attack of increasing lift. At high angles of attack near that of maximum lift, strong trailing-edge vorticity is measured under the windward tip vortex, which increases in magnitude with the lift off of the tip vortex from the trailing edge of the wing. This action reduces the stabilizing roll moments at angles of attack near that of maximum lift.

Flow features such as unsteady leading-edge flow reattachment and both the spatial growth, strengthening, and lift off of the tip vortex highlight the sensitivity of the lateral stability of LAR wings to the many elements of their design (e.g., planform geometry, geometric twist, wing planarity). While this paper provided initial insights into the flow physics behind the static lateral stability characteristics of LAR rectangular wings, more work is needed on other planform geometries in an effort to identify key effectors of the lateral stability of LAR wings at angles of attack involving separated flow. In the end, these pursuits will improve the vehicle and control design of LAR fliers, enabling higher levels of maneuverability in an expanded flight envelope.

ACKNOWLEDGMENTS

The authors acknowledge the partial financial support of the Air Force Office of Scientific Research (AFOSR). The authors also wish to thank the anonymous reviewers for their time as well as Dr. A. C. DeVoria for enlightening discussions.

[1] P. Freymuth, F. Finaish, and W. Bank, Visualization of wing tip vortices in accelerating and steady flow, J. Aircr. **23**, 730 (1986).

[2] K. Taira and T. Colonius, Three-dimensional flows around low-aspect-ratio flat-plate wings at low Reynolds numbers, J. Fluid Mech. **623**, 187 (2009).

[3] K. Taira and T. Colonius, Effect of tip vortices in low-Reynolds-number poststall flow control, AIAA J. **47**, 749 (2009).

[4] T. O. Yilmaz and D. Rockwell, Flow structure on finite-span wings due to pitch-up motion, J. Fluid Mech. **691**, 518 (2012).

[5] T. O. Yilmaz and D. Rockwell, Three-dimensional flow structure on a maneuvering wing, Exp. Fluids **48**, 539 (2010).

[6] M. R. Visbal, Unsteady flow structure and loading of a pitching low-aspect-ratio wing, Phys. Rev. Fluids **2**, 024703 (2017).

[7] M. R. Visbal, Three-dimensional flow structure on a heaving low-aspect-ratio wing, in *Proceedings of the 49th AIAA Aerospace Sciences Meeting*, 2011-219 (American Institute of Aeronautics and Astronautics, Orlando, FL, 2011), pp. 1–24.

[8] M. Okamoto and A. Azuma, Aerodynamic characteristics at low Reynolds numbers for wings of various planforms, AIAA J. **49**, 1135 (2011).

[9] D. R. Morse and J. A. Liburdy, Vortex dynamics and shedding of a low aspect ratio, flat wing at low Reynolds numbers and high angles of attack, ASME: J. Fluids Eng. **131**, 1 (2009).

[10] E. C. Polhamus, *A Concept of the Vortex Lift of Sharp-Edge Delta Wings Based on a Leading-Edge Suction Analogy*, Technical Report TN D-3767 (NASA, Langley Research Center, Hampton, VA, 1966).

[11] Y. Lian, W. Shyy, D. Viieru, and B. Zhang, Membrane wing aerodynamics for micro air vehicles, Prog. Aerospace Sci. **39**, 425 (2003).

[12] J. E. Lamar, *Extension of Leading-Edge Suction Analogy to Wings with Separated Flow Around the Side Edges at Subsonic Speeds*, Technical Report TR R-428 (NASA, Langley Research Center, Hampton, VA, 1974).

[13] G. E. Torres and T. J. Mueller, Low-aspect-ratio wing aerodynamics at low Reynolds numbers, AIAA J. **42**, 865 (2004).

[14] P. Cosyn and J. Vierendeels, Numerical investigation of low-aspect-ratio wings at low Reynolds numbers, J. Aircr. **43**, 713 (2006).

[15] B. Carmichael, *Low Reynolds Number Airfoil Survey*, NASA CR 165803, Vol. 1, Purchase Order L-4059B (Langley Research Center, National Aeronautics and Space Administration (NASA), 1981).

[16] M. S. Selig, J. F. Donovan, and D. B. Fraser, *Airfoils at Low Speeds* (Stokely, Virginia Beach, VA, 1989).

[17] W. G. Bastedo and T. J. Mueller, Spanwise variation of laminar separation bubbles on wings at low Reynolds numbers, J. Aircr. **23**, 687 (1986).

[18] A. Pelletier and T. J. Mueller, Low Reynolds number aerodynamics of low-aspect-ratio, thin/flat/cambered-plate wings, J. Aircr. **37**, 825 (2000).

[19] G. K. Ananda, P. P. Sukumar, and M. S. Selig, Measured aerodynamic characteristics of wings at low Reynolds numbers, Aerosp. Sci. Technol. **42**, 392 (2015).

[20] H. Winter, Flow phenomena on plates and airfoils of short span, NASA TM 798 (National Advisory Committee for Aeronautics, Washington, DC, 1936).

[21] A. C. DeVoria and K. Mohseni, On the mechanism of high-incidence lift generation for steadily translating low-aspect-ratio wings, J. Fluid Mech. **813**, 110 (2017).

[22] S. Watkins, J. Milbank, B. J. Loxton, and W. H. Melbourne, Atmospheric winds and their implications for micro air vehicles, AIAA J. **44**, 2591 (2006).

[23] M. Shields and K. Mohseni, Effects of sideslip on the aerodynamics of low aspect ratio wings at low Reynolds numbers, AIAA J. **50**, 85 (2012).

[24] M. J. Queijo, *Theoretical Span Load Distributions and Rolling Moments for Sideslipping Wings of Arbitrary Plan Form in Incompressible Flow*, NACA TN 3605 (National Advisory Committee for Aeronautics, Langley Field, VA, 1955).

[25] A. C. DeVoria and K. Mohseni, A vortex model for forces and moments on low-aspect-ratio wings in side-slip with experimental validation, Proc. R. Soc. London A **473** (2017).

[26] L. E. Ericssson, The fluid mechanics of slender wing rock, J. Aircr. **21**, 322 (1984).

[27] J. Katz, Wing/vortex interactions and wing rock, Prog. Aerospace Sci. **35**, 727 (1999).

[28] M. Shields and K. Mohseni, Inherent stability modes of low aspect ratio wings, J. Aircr. **52**, 141 (2015).

[29] M. Shields and K. Mohseni, Roll stall for low-aspect-ratio wings, J. Aircr. **50**, 1060 (2013); **53**, 1186(E) (2016).

[30] J. R. Johnson, S. Grafton, and L. Yip, Exploratory investigation of the effects of vortex bursting on the high angle-of-attack lateral-directional stability characteristics of highly-swept wings, in *Proceedings of the AIAA Aerodynamic Testing Conference* (Colorado Springs, CO, 1980).

[31] D. Levin and J. Katz, Dynamic load measurements with delta wings undergoing self-induced roll oscillations, J. Aircr. **21**, 30 (1984).

[32] S. M. Soloff, R. J. Adrian, and Z. C. Liu, Distortion compensation for generalized stereoscopic particle image velocimetry, Meas. Sci. Technol. **8**, 1441 (1997).

[33] C. Willert, Stereoscopic digital particle image velocimetry for application in wind tunnel flows, Meas. Sci. Technol. **8**, 1465 (1997).

[34] B. Wieneke, Stereo-PIV using self-calibration on particle images, Exp. Fluids **39**, 267 (2005).

[35] M. Raffel, C. E. Willert, and J. Kompenhans, *Particle Image Velocimetry* (Springer-Verlag, New York, 1998).

[36] L. Graftieaux, M. Michard, and N. Grosjean, Combining PIV, POD and vortex identification algorithms for the study of unsteady turbulent swirling flows, Meas. Sci. Technol. **12**, 1422 (2001).

[37] S. M. Kaplan, A. Altman, and M. Ol, Wake vorticity measurements for low-aspect-ratio wings at low Reynolds number, J. Aircr. **44**, 241 (2007).

[38] J. D. Anderson, Jr., *Fundamentals of Aerodynamics*, 3rd ed. (McGraw-Hill, Boston, 2001).

[39] P. L. Coe, Jr., A. B. Graham, and J. R. Chambers, *Summary of Information on Low-Speed Lateral-Directional Derivatives Due to Rate of Change of Side-Slip* $\dot{\beta}$, NASA TN D-7972 (Langley Research Center, National Aeronautics and Space Administration, Hampton, VA, 1975).

[40] S. P. Fears, H. M. Ross, and T. M. Moul, *Low-Speed Wind-Tunnel Investigation of the Stability and Control Characteristics of a Series of Flying Wings with Sweep Angles of* 50°, NASA TM 4640 (Langley Research Center, National Aeronautics and Space Administration, Hampton, VA, 1995).

[41] T. M. Moul, S. P. Fears, H. M. Ross, and J. V. Foster, *Low-Speed Wind-Tunnel Investigation of the Stability and Control Characteristics of a Series of Flying Wings with Sweep Angles of* 60°, NASA TM 4649 (Langley Research Center, National Aeronautics and Space Administration, Hampton, VA, 1995).

[42] H. M. Ross, S. P. Fears, and T. M. Moul, *Low-Speed Wind-Tunnel Investigation of the Stability and Control Characteristics of a Series of Flying Wings with Sweep Angles of* 70°, NASA TM 4671 (Langley Research Center, National Aeronautics and Space Administration, Hampton, VA, 1995).

[43] T. Hu, Z. Wang, and I. Gursul, Passive control of roll oscillations of low-aspect-ratio wings using bleed, Exp. Fluids **55**, 1752 (2014).